Permeability and fluid flow-induced wall shear stress in bone scaffolds with TPMS and lattice architectures: A CFD analysis

Davar Ali, Mehmet Ozalp, Sebastien B.G. Blanquer, Selis Onel

▶ To cite this version:

HAL Id: hal-02428552

https://hal.umontpellier.fr/hal-02428552

Submitted on 10 Dec 2020

Journal Pre-proof

Permeability and fluid flow-induced wall shear stress in bone scaffolds with TPMS and lattice architectures: A CFD analysis

Davar Ali, Mehmet Ozalp, Sebastien B.G. Blanquer, Selis Onel

Please cite this article as: D. Ali, M. Ozalp, S.B.G. Blanquer et al., Permeability and fluid flow-induced wall shear stress in bone scaffolds with TPMS and lattice architectures: A CFD analysis, *European Journal of Mechanics / B Fluids* (2019), doi: https://doi.org/10.1016/j.euromechflu.2019.09.015.

This is a PDF file of an article that has undergone enhancements after acceptance, such as the addition of a cover page and metadata, and formatting for readability, but it is not yet the definitive version of record. This version will undergo additional copyediting, typesetting and review before it is published in its final form, but we are providing this version to give early visibility of the article. Please note that, during the production process, errors may be discovered which could affect the content, and all legal disclaimers that apply to the journal pertain.

Permeability and Fluid Flow-Induced Wall Shear Stress in Bone Scaffolds with TPMS and Lattice Architectures: A CFD Analysis

Davar Ali[a], Mehmet Ozalp[b], Sebastien B G Blanquer[c], Selis Onel [d,*]

[a]Karabuk University, Department of Medical Engineering, Karabuk, Turkey, daverali@karabuk.edu.tr

[b]Karabuk University, Department of Mechanical Engineering, Karabuk, Turkey, mozalp@karabuk.edu.tr

[c]Institute Charles Gerhardt Montpellier, CNRS - University of Montpellier - ENSCM, 34095 Montpellier, Cedex 5, France, sebastien.blanquer@umontpellier.fr

[d]Hacettepe University, Department of Chemical Engineering, Ankara, Turkey, selis@hacettepe.edu.tr

[*]Corresponding author: Selis Onel, Hacettepe University, Department of Chemical Engineering, Beytepe, Ankara 06800, Turkey, selis@hacettepe.edu.tr, +90 (532) 464 7911 c., +90 (312) 297 7401 o.

Abstract

Fluid flow dynamics within porous scaffolds for tissue engineering play a critical role in the transport of fundamental materials to the cells and in controlling the biocompatibility of the scaffold. Properties such as permeability and fluid flow-induced wall shear stress characterize the biological behavior of the scaffolds. Bioactivity depends on the diffusion of oxygen and other nutritious elements through the porous medium and fluid flow-induced shear stress is known as the dominant mechanical stimulant of cell differentiation and proliferation within the scaffolds. In this study, eight different bone scaffold models with a constant porosity of 80% were designed computationally using the TPMS and lattice-based structures. We investigated the fluid flow within the scaffolds using CFD analysis. The results of the work showed that scaffold architecture has a significant impact on the permeability and that scaffold permeability can vary up to three times depending on the architecture. The scaffolds with the minimal variation in their channel size exhibited the highest permeability. We investigated the distribution statistics of wall shear stress on the walls of the scaffolds and showed that a correlation between the architecture of the scaffolds and the distribution statistics of wall shear stress did not exist. The outcomings of this work can be promising in designing better scaffolds in tissue engineering from a biological point of view.

Keywords: Bone scaffolds; Permeability; Wall shear stress; Minimal surface architectures; Lattice-based architectures

1. Introduction

Culturing cells from the patient in scaffolds before their actual implantation into tissues is a promising approach that can accelerate the treatment process [1]. Stem cells have been used extensively in such processes for differentiation to other phenotypes [2, 3] due to their ability to respond to both biochemical and biophysical cues around them. The phenotype of stem

cells can be regulated depending on the signals they receive [4, 5]. Biophysical signals involve those that arise from the changes in the mechanical properties of the matrix and substrate, such as strain and stiffness, substrate topography, hydrostatic pressure, fluid flow-induced shear stress, and electromagnetic field [6-8].

Wall shear stress (WSS) plays a significant role in the differentiation and proliferation of cells in perfusion bioreactors that include relatively more dynamic cell culture systems [9]. Differences in shear stress create a ubiquitous environmental signal that can be sensed by stem cells during differentiation or circulation in a perfusion bioreactor [10]. The contribution of shear stress to the differentiation of pluripotent stem cells toward endothelial [11], cardiac [12], hematopoietic [13], and osteoblast [14] phenotypes has been widely reported. A study on the role of WSS during the initial deposition of cells on the scaffolds [15] has shown that local WSS is the main factor controlling the extent of cell deposition, which is strongly influenced by the architecture of the pore network of the scaffold. Evaluation of the degradable behaviors of scaffolds, specifically of biodegradable polymers employed as implants in the body, is another important issue for clinical applications. Studies on the degradation effects of flow behavior of fluids in polymeric scaffolds of varying porosity and permeability have shown that lower values of porosity and permeability caused higher rates of degradation with shorter scaffold life due to higher initial stiffness [16]. Therefore, determining and prediction of fluid flow-induced shear stress on the walls of a scaffold can be an effective step in controlling the perfusion in cell culture processes.

WSS is defined as the force per unit area applied by the wall surface on the fluid in a direction on the local tangent plane [17]. Its measurement is not practical due to the need for embedding very sensitive sensors on the walls [18, 19]. This difficulty becomes more critical in the case of tissue scaffolds that possess a porous structure in the micro scale [20, 21]. Computational simulations of biomaterials have recently gained significant attention with the

capacity to provide immediate results as an alternative and economical approach compared to experimental analyses [22, 23]. Numerous computational fluid dynamics (CFD) analyses have been conducted to evaluate the permeability and WSS of various types of scaffolds [15, 24-26]. Lesman and et al. employed CFD simulations to show that cellular growth within 3D scaffolds caused the WSS to increase due to contraction in the channels of the scaffolds during perfusion cell culturing [27]. Zhao et al. studied the parametric impacts of the geometric features of scaffolds, such as architecture, pore size, and porosity on the WSS in the pores employing a fluid–structure interaction model for various cases of loading during fluid perfusion, mechanical compression, as well as a combination of the two [28]. Their results showed that specifically pore size substantially influenced the mechanical stimulation within the scaffold and combined application of fluid perfusion with mechanical load amplified the WSS significantly. Marin and Lacroix examined the effects of inter-sample structural variability of regular scaffolds on the magnitude and distribution of WSS using CFD calculations [24]. Their results showed that geometric inconsistencies instigated high variability in velocity and WSS among the samples.

Another parameter that plays an important role in the success of scaffolds is their intrinsic permeability [23]. A permeable scaffold should allow for unhindered flow and diffusion of cell culture media through its pores in order to supply oxygen and nutrition to the cells [29]. Prediction of the permeability in scaffolds using computational simulations is a common practice in tissue engineering [20, 26]. In a previous study, we conducted a finite element analysis to identify and compare the effects of two different structures, namely gyroid and rectangular lattice structures, on the permeability, fluid-induced WSS, elastic modulus, and compressive strength in highly porous scaffolds. Our results signified the potent effects of porosity on the permeability and the WSS, where higher porosity caused the permeability to increase while WSS, elastic modulus, and compressive strength values decreased [21].

In the design of bone scaffolds, the common goal in general is to mimic the structure of the trabecular (cancellous or spongy) bone [30] found in the human body. The trabecular bone has a greatly porous structure, accordingly, the design of high porosity scaffolds is the main criterion in bone tissue engineering. In response to this necessity of bone scaffolds, the triply periodic minimal surface (TPMS) and the lattice-based architectures are the two groups of scaffolds that are used widely [21, 31]. However, the effects of geometrical parameters on the permeability and WSS for different scaffold architectures are critical and still remain less understood due to the diversity of scaffold structures. Therefore, analyzing and comparing the permeability and WSS of these two groups of scaffolds can be a very effective step in selecting and designing bone scaffolds.

In this study, we built eight different scaffolds computationally with a constant porosity of 80%. We used the TPMS and lattice-based structures with each based on four different geometries. These scaffolds were then exploited for quantification of their permeability and WSS using CFD analysis.

2. Materials and Methods

2.1. Scaffold models

Total of eight scaffolds were designed using the SolidWorks 2017 software. Four of the scaffolds were built in the lattice-based architecture using one of the double-diamond, truncated-octahedron [32], octet [33] and one optimized-lattice [34] structures. A strut size of 200 µm was selected for the scaffolds [35]. The other four scaffolds were designed using the TPMS architecture in one of the double-diamond [36], gyroid [37], schwarz-primitive [38] and F-RD [39] type geometries. The primary surfaces in TPMS scaffolds were created using the k3dsurf (k3dsurf.sourceforge.net) software application, which has the capability of visualizing parametric equations in 3-D and more. The outputs of this software, in the form of mesh files with .obj extension, were imported to the SolidWorks software and were thickened

geometrically to obtain the desired porosity. A wall thickness of 100 µm was selected for TPMS scaffolds [21]. Trigonometric functions of x, y and z that were used in building the TPMS scaffold structures are shown in table 1.

TABLE 1 Parametric equations for TPMS structures

TPMS architecture	Equations f (x,y,z)=0
Gyroid	$\cos(x)\cdot\sin(y)+\cos(y)\cdot\sin(z)+\cos(z)\cdot\sin(x)$
Schwarz primitive	$\cos(x)+\cos(y)+\cos(z)$
Double diamond	$\cos(x)\cdot\cos(y)\cdot\cos(z)-\sin(x)\cdot\sin(y)\cdot\sin(z)$
F-RD	$3[\cos(x)+\cos(y)+\cos(z)]+8[\cos(x)\cdot\cos(y)\cdot\cos(z)]$

The model unit cells were repeated in the direction of the three axes (x, y, and z) four times to obtain a cubic model made-up of 64 unit cells of any of the architectures listed. Fluid domains in the 3-D structures were obtained by subtracting the geometrical parts from an enclosing box. All eight unit cells employed are isometric and have symmetric architecture in the x, y, and z axes. The geometrical parameters of the unit cells are presented in table 2. Figure 1 shows a representative picture of each scaffold created in this study including the unit cell and the corresponding 3-D structure with the solid and fluid domains.

TABLE 2 Geometrical parameters for the lattice-based and TMPS scaffold models. L, s, D, and d represent the model size, unit cell length, pore size in the widest area and pore size in the narrowest area, respectively.

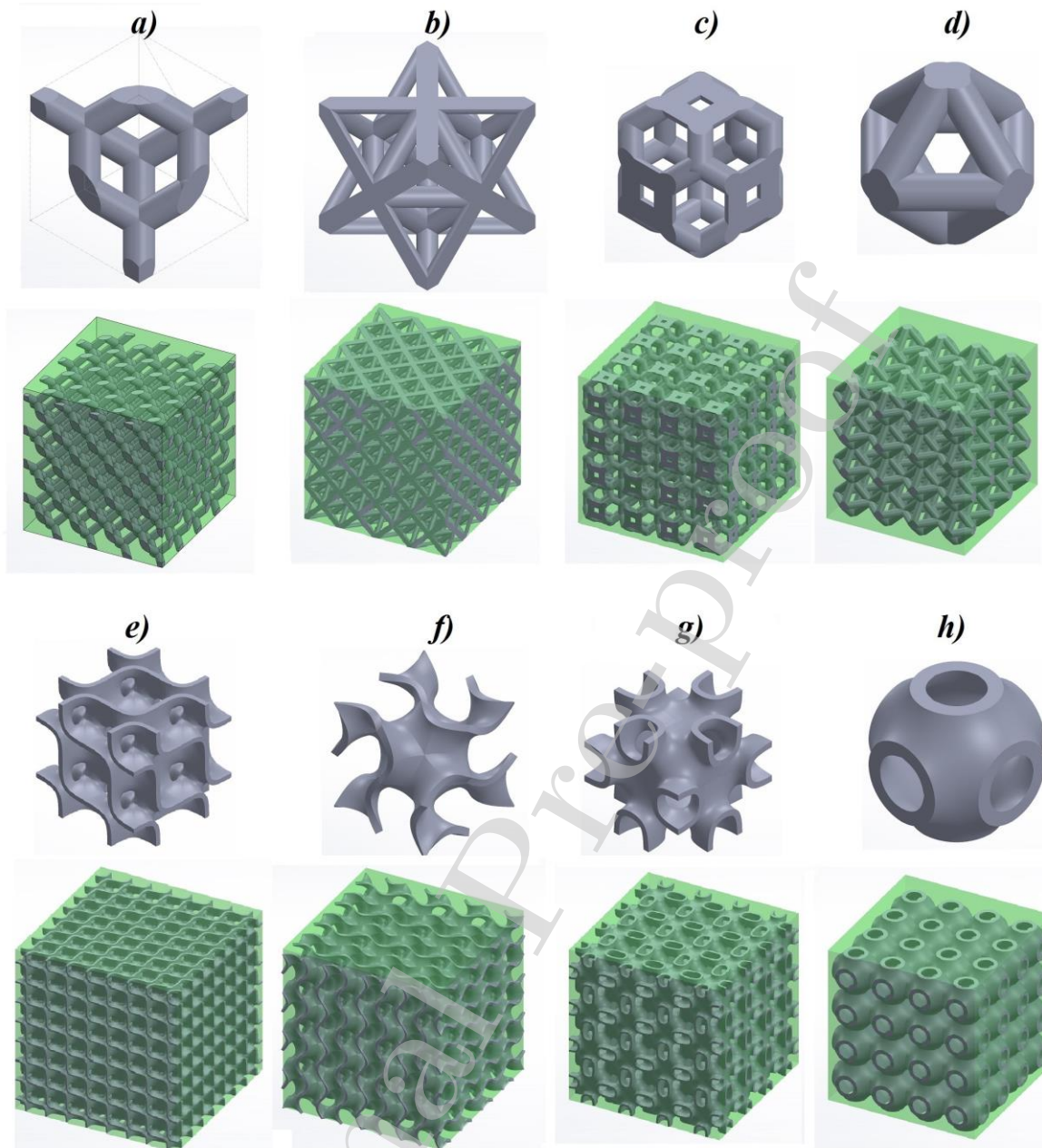| Model parameters (mm)	Lattice-based scaffolds				TPMS scaffolds Length in x, y, z calculated in $[-\pi, \pi]$ boundary			
	Lattice-diamond	Truncated-octahedron	Octet	Optimized-lattice	Double-diamond	Gyroid	Schwarz primitive	F-RD
L	3.80	4.64	5.60	4.00	10.16	6.24	4.00	7.36
S	0.95	1.16	1.40	1.00	2.54	1.56	1.00	1.84
D	0.49	0.80	0.79	0.51	1.17	0.68	0.90	0.48
D	0.49	0.15	0.33	0.20	0.20	0.68	0.40	0.39

FIGURE 1 The unit cells and the corresponding 3-D scaffolds with the solid (gray) and fluid (green) domains for the following structures: a) Lattice-diamond, b) Octet, c) Truncated-octahedron, d) Optimized-lattice, e) Double-diamond, f) Gyroid, g) FR-D, and h) Schwarz primitive.

2.2. Governing equations in CFD analysis

Navier-Stokes relation for fully developed flow of an incompressible fluid with constant density and viscosity was used in the CFD analysis [40]:

$$\rho \frac{\partial u}{\partial t} - \mu \nabla^2 u + \rho(u.\nabla)u + \nabla p = F, \quad \nabla.u = 0 \tag{1}$$

where ρ, u, and μ represent the density (kg/m^3), velocity (m/s), and the dynamic viscosity of fluid (kg/m.s). ∇ denotes the del operator and p denotes the pressure (Pa). F represents the forces, such as gravity and centrifugal force, where F = 0 in the specific problem studied here [40, 41].

WSS, represented by τ_ω, is the tangential drag force exerted by the fluid flowing across the surface of the scaffolds [42] and is given by:

$$\tau_\omega = \mu \frac{\partial u}{\partial h} \tag{2}$$

where *u* denotes the flow velocity and *h* represents the x-, y-, and z-directions [43].

Permeability, k, of the scaffolds was calculated using Darcy's law [23]:

$$k = \frac{Q\mu L}{A\Delta P} \tag{3}$$

where Q, L, μ, A, and ΔP represent the inlet fluid flow rate (m^3/s), dynamic fluid viscosity (kg/m.s), model length (m), inlet cross section area (m^2), and pressure drop (Pa), respectively.

2.3. Fluid properties and boundary conditions in CFD

A 1000 kg/m^3 density and a 0.0037 Pa.s dynamic viscosity (for cell culture media with 5% wt/wt dextran) were assigned to the fluid properties [44]. We assumed an entirely liquid cell culture media with no solid particles for ease of calculations. The inlet velocity was selected as 0.1 mm/s suitable for flow in bone scaffolds. The walls of the scaffolds were assumed to be hydrophilic and the no-slip condition was applied [26, 45]. The outlet gauge pressure was adopted as zero [24, 26, 27] (Figure 2). The pressure drop ΔP used in equation (3) to calculate the permeability and WSS of the scaffolds was computed using the Ansys Fluent software.
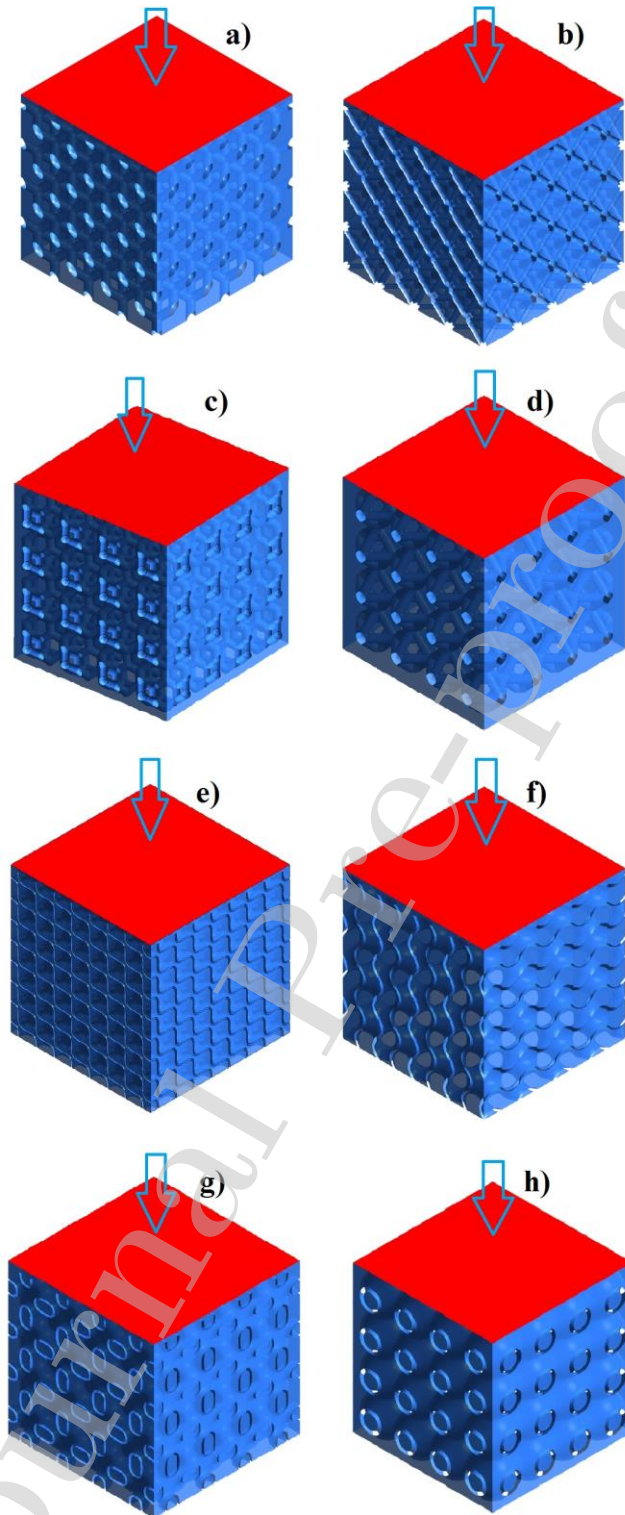
FIGURE 2 A velocity of 0.1 mm/s and no-slip boundary condition were assigned at the inlet (red) and at the walls (blue), respectively, for the a) lattice-diamond, b) octet, c) truncated-octahedron, d) optimized-lattice, e) double-diamond, f) gyroid, g) FR-D, and h) Schwarz-primitive structures.

CFD analysis was performed assuming steady-state fluid flow in 3-D scaffold geometries that were meshed using tetrahedral elements [23]. In order to ensure the independence of the results to mesh size, the sensitivity of the pressure drop in the inlet to the number of elements for each model was analysed. Table 3 represents the number of elements in each scaffold. The residual sensitivity criterion for convergence was set as 1e-5.

TABLE 3 Number of elements in each scaffold in the CFD models

Lattice-diamond	Truncated-octahedron	Octet	Optimized-lattice	Double-diamond	Gyroid	Schwarz-primitive	F-RD
5645734	9107611	17549250	8341502	1441009	14658043	5062830	10989006

3. Results

3.1. Fluid flow dynamics within scaffolds

Simulation results for pressure profile in all scaffold geometries have shown that the highest pressure occurred in the inlet and gradually tended to zero in the outlet region confirming the boundary conditions used in the models. Figure 3 illustrates the pressure profile within the 3-D geometries in the counter format.

Generally, the exerted pressure in lattice-based scaffolds is lower than that observed in TPMS models. An intra-group comparison in lattice-based scaffolds showed that the highest pressure was observed in the octet model and the lowest was observed in the optimum-lattice model. Amongst the geometries used in the TPMS scaffolds group, the highest pressure was observed in the double-diamond structure while the lowest was marked in the gyroid model.
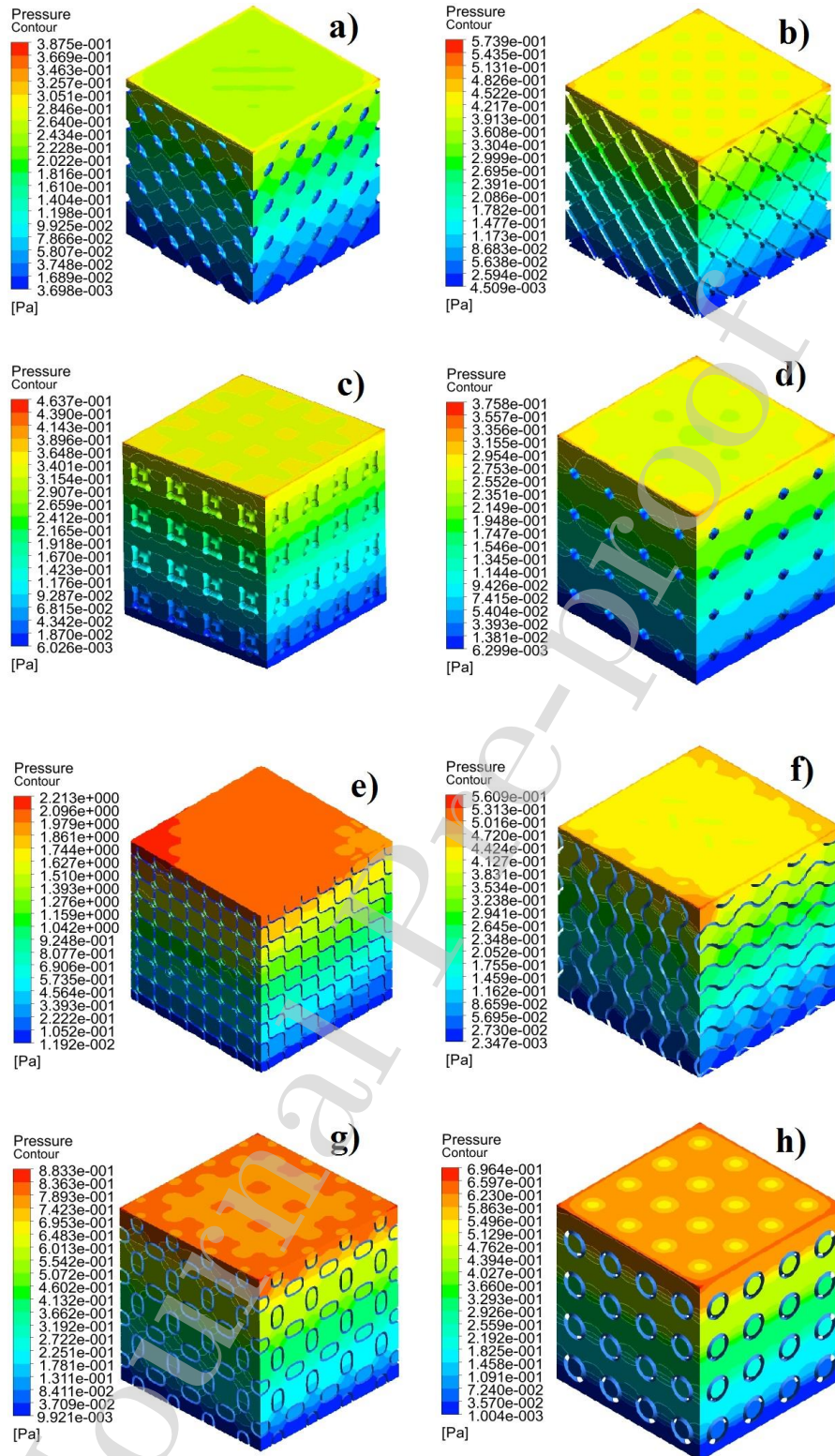
FIGURE 3 3-D simulation results showing pressure profiles in counter form for a) lattice-diamond, b) octet, c) truncated-octahedron, d) optimized-lattice, e) double-diamond, f) gyroid, g) FR-D, and h) Schwarz-primitive scaffolds using an inlet velocity of 0.1 mm/s.

To determine the reliability and precision of the CFD models, their pressure drop, ΔP, responses to the changes in inlet velocity were investigated for four different inlet velocities, namely 0.1, 0.25, 0.5, and 1 mm/s [26]. Figure 4 illustrates the logarithmic curve-fitting plots of the assigned inlet velocity and the ΔP obtained for each of the models. In all scaffolds, the pressure drop correlated extremely well with the inlet velocity with $R^2 > 0.999$.
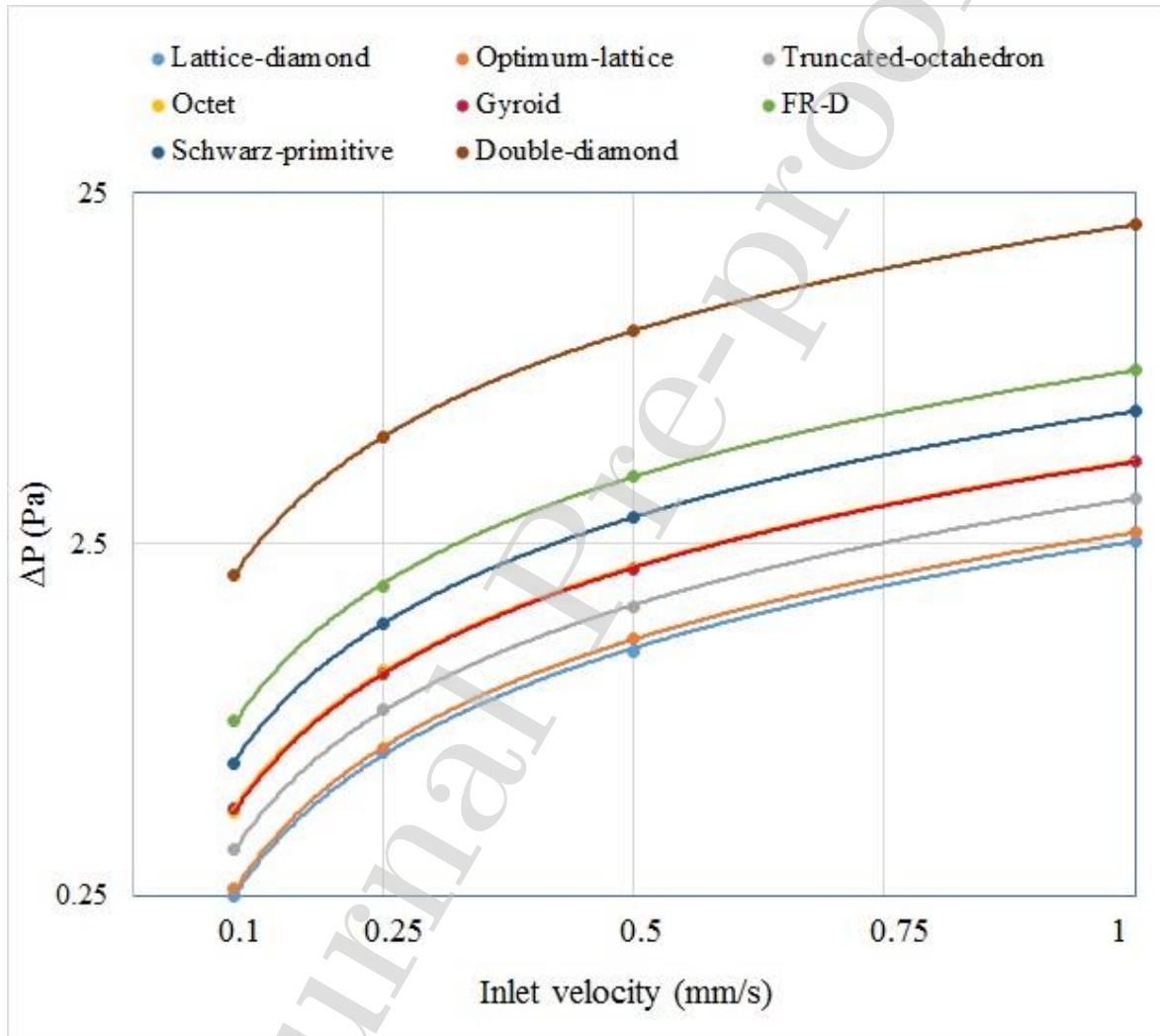

FIGURE 4 Correlation between assigned inlet velocity and calculated ΔP in the scaffolds.

3.2. Permeability

The permeability of each scaffold was calculated with reference to the average ΔP at the inlet derived from the CFD models and Darcy's law using equation (3). Figure 5 shows the calculated permeability values for each scaffold.
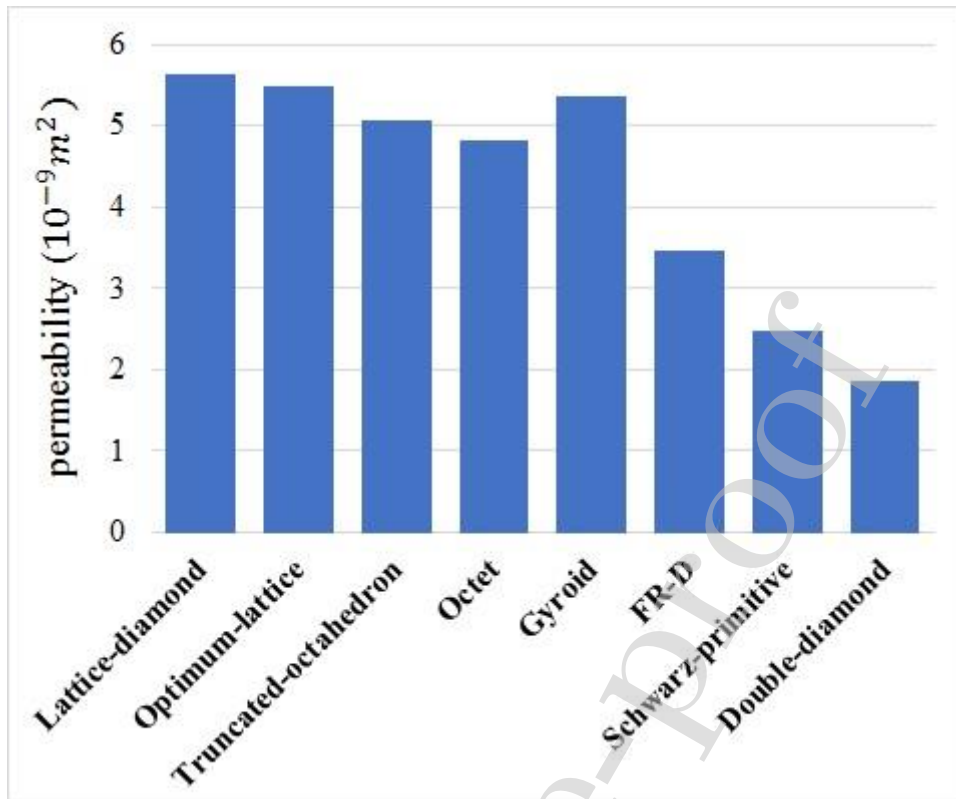
FIGURE 5 Calculated permeability of each scaffold using Darcy's law.

For the case of similar porosity, lattice-based scaffolds showed substantially higher permeability than did the TPMS models except for the gyroid architecture. To validate the CFD results, the permeability value obtained for the gyroid model in this study as $5.36*10^{-9}$ m^2 was compared to that ($6.7*10^{-9}$ m^2) derived in our previous work [21] using only two unit-cells with the periodic boundary condition. The difference found was about 25%, which was caused by an underestimation of the magnitude of the pressure drop in the previous model by using limited number of unit-cells.

3.3. WSS

The WSS profile contours on the walls within all scaffolds are shown in Figure 6. Given that the WSS changes linearly with the velocity gradient (equation 2), the maximum WSS was found to occur along the narrower regions of the channels in the scaffold causing higher fluid flow rates. For all models, the calculated maximum WSS varied between 41.5 and 81.4 mPa.
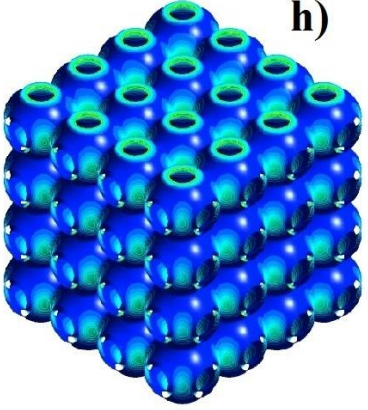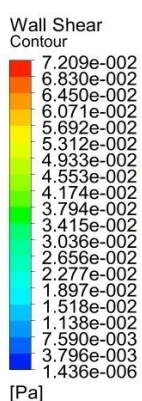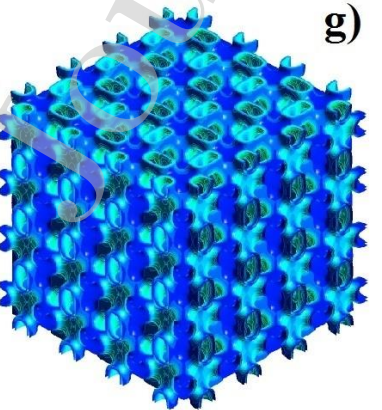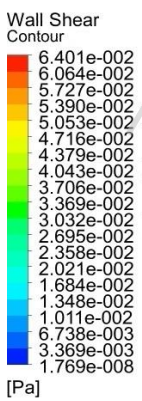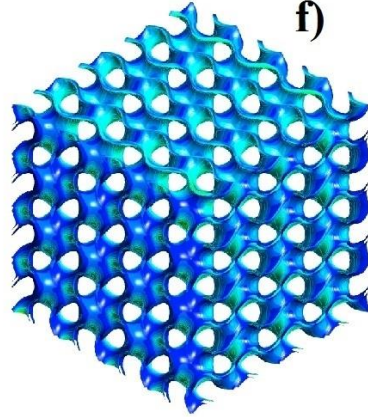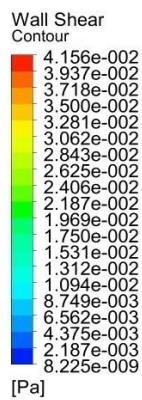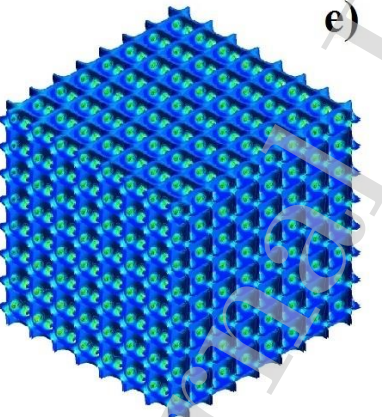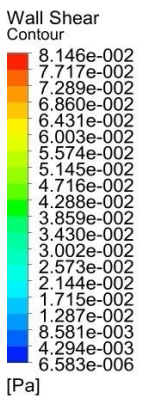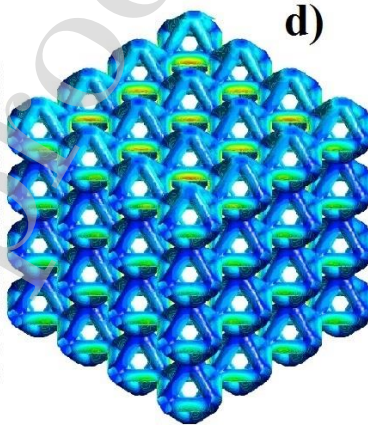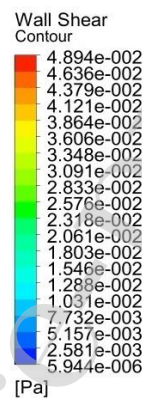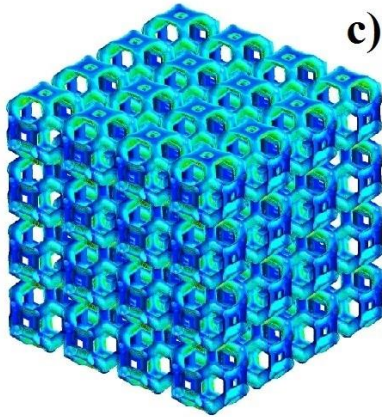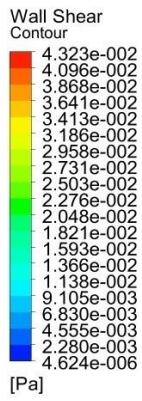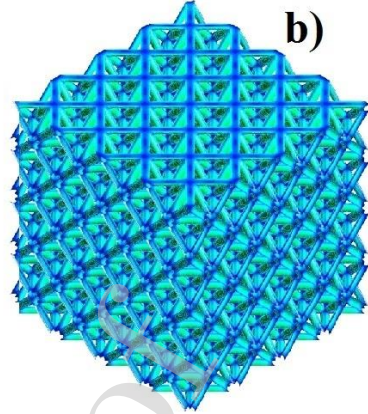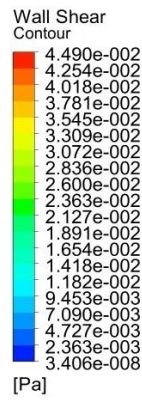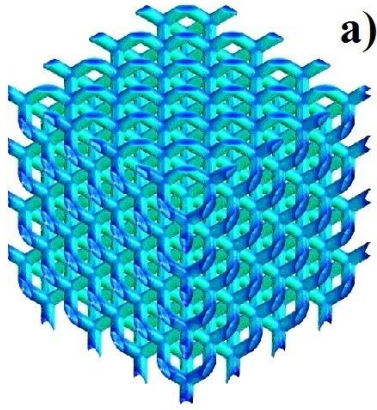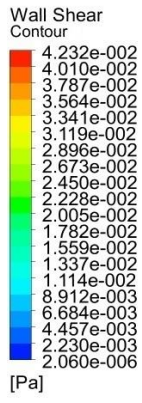
FIGURE 6 WSS contours for the a) lattice-diamond, b) octet, c) truncated-octahedron, d) optimized-lattice, e) double-diamond, f) gyroid, g) FR-D and h) schwarz-primitive structure.

The maximum WSS values obtained for the lattice-based scaffolds, with the exception of the gyroid model, were relatively smaller than those obtained for the TPMS models. The average WSS values for all the scaffolds are illustrated in Figure 7. The highest value of average WSS was found as 13.76 mPa, much higher relative to other models, for the double-diamond model, which is a TPMS type architecture.
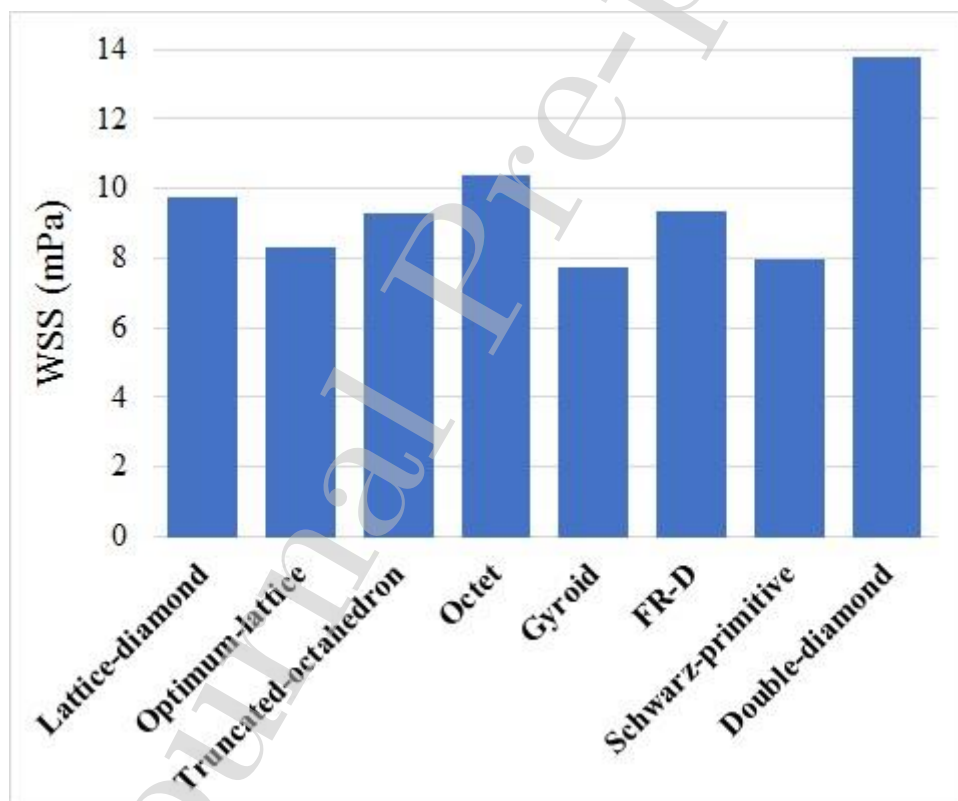
FIGURE 7 Calculated values of average WSS in scaffolds with eight different structures induced by an inlet velocity of 0.1 mm/s.

The range of average WSS values that would initiate osteogenic differentiation of mesenchymal stem cells (MSC) used in the literature [28] is between 0.1–10 mPa and an average WSS smaller than 15 mPa is often recommended for differentiation of MSCs to osteoblasts and osteocytes in perfusion bioreactor culture systems [46-48].

4. Discussion

In this work, we conducted a computational study to understand the effects of scaffold architecture on the permeability and WSS using eight different models with the same porosity (80%). The calculated values of the permeability were in the range of $1.85 - 5.62 \times 10^{-9} m^2$. These results are in agreement with the value, $5.13 \times 10^{-9} m^2$, that has been found for human trabecular bone permeability [49]. Although porosity is usually described as the main factor affecting the permeability of scaffolds [23, 29, 50], the results of this study suggest that under the condition of similar porosity, scaffold geometry is another important factor.

The simulation results shown in Figure 5 indicate that the permeability of the lattice-diamond model is three times as large as that of the double-diamond scaffold calculated at the same porosity. This concludes that the permeability of scaffolds is highly dependent on their architecture as well as on their porosity. Table 4 provides the differences in the geometric parameters in dimensionless form used for each of the eight scaffolds in this study, which can be used to understand the substantial discrepancy in the calculated permeability of scaffolds with different architectures. *D/*d represents the ratio of the widest pore size to the narrowest and *A/*A_0 represents the ratio of the area with no obstacles to the total inlet area. The area with no obstacles within the scaffolds can be described as the cross-sectional area, through which the fluid flows from inlet to outlet without encountering any walls.

TABLE 4 Architectural parameters in dimensionless form and the respective calculated permeability for each scaffold-geometry

Model	Lattice-diamond	Octet	Optimized-lattice	Truncated-octahedron	Double-diamond	F-RD	Schwarz-primitive	Gyroid
D/d	1.00	2.38	2.56	5.26	5.88	3	2.27	1
A/A_0 (%)	15.68	9.10	30.60	35.00	0.00	4.80	21.50	10.63
Permeability $(10^{-9}m^2)$	5.62	4.81	5.48	5.06	1.85	3.46	2.48	5.36

As it can be seen in Table 4, the highest permeability value was found for the lattice-diamond structure while the lowest value was obtained for the double-diamond model, which possess the lowest and the maximum D/d values, respectively. Therefore, it can be concluded that increasing the extent of variations in the channel size, which implies an increase in tortuosity, in the TPMS scaffolds, has caused their permeability to decrease. Accordingly, it is logical to expect that the octet model will be the second most permeable scaffold amongst the lattice-based group of scaffolds, but on the contrary it is found to possess the lowest permeability amongst them. This is where the ratio given by A/A_0 needs to be considered as the second factor affecting the permeability of the scaffolds. The octet model, due to its very low value of A/A_0, presented the minimum permeability amongst the lattice-based scaffolds. With regards to both groups of scaffolds, the results imply that the scaffold permeability was primarily affected by any variations in the channel size. The existence and/or absence of straight-gaps along the flow streamline between the inlet and outlet locations was the second factor affecting the scaffold permeability.

It is previously shown that a heterogeneous WSS distribution causes non-uniform cell differentiation within the scaffolds [24, 27, 42]. Therefore, understanding the distribution statistics of WSS on the scaffolds is crucial and necessary. The distribution curves and modality of WSS with respect to the percent area of the walls in the eight scaffolds with different architectures are shown in Figure 8.
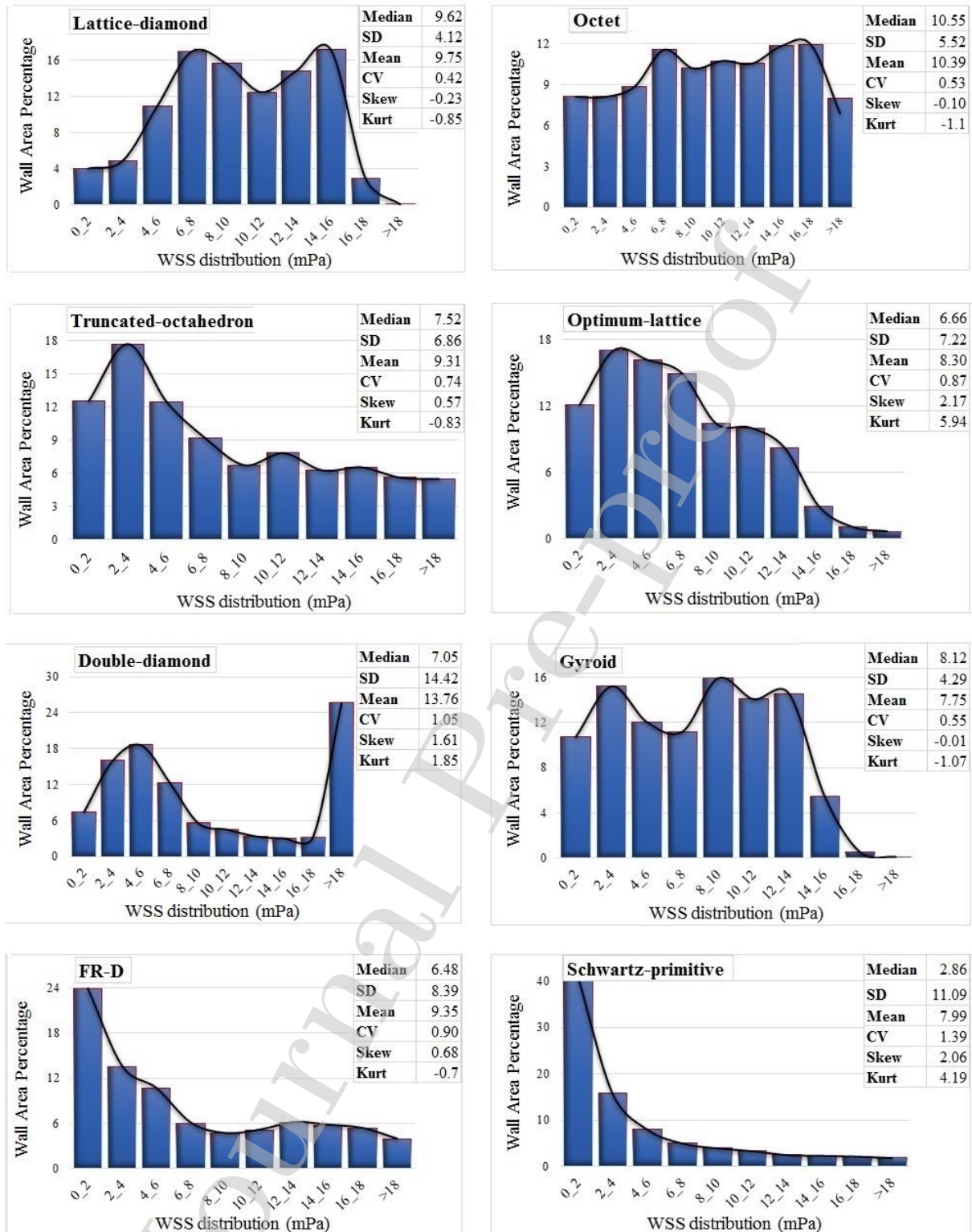
FIGURE 8 Histograms for WSS distribution in scaffolds with eight different architectures, where SD, CV, Skew, and Kurt represent the standard deviation, coefficient of variance, skewness, and kurtosis of the WSS distribution curves.

A coefficient of variance larger than zero in all models showed that the WSS was not distributed equally in any of the models (Figure 8). Amongst the models in both the TPMS and lattice-based architecture groups, the lattice-diamond model with the lowest coefficient of variance (0.42) showed a relatively more equal distribution of the WSS on the walls of the scaffold and the Schwartz-primitive model with the highest coefficient of variance (1.39) showed a relatively less uniform distribution of WSS.

A skewness value that is higher than zero indicates that WSS values greater or smaller than the mean WSS were not distributed symmetrically and that the relative sizes of the two tails of the distribution curve are not similar. The gyroid model, which showed very small skewness (-0.01), presented a relatively more symmetrical WSS distribution than did the other scaffolds.

Kurtosis measures the tail-heaviness of a distribution and the calculated kurtosis values in Figure 8 shows the range of variation in WSS values in the scaffolds. The optimum-lattice and FR-D models with kurtoses of 5.94 and -0.7 indicate the heaviest and lightest tails in the WSS distribution, respectively. In other words, the FR-D model, compared to the other models, suggests a smaller range of WSS values.

In an overview of the permeability results, as well as the WSS distribution statistics (modality, standard deviation, coefficient of variance, skewness, and kurtosis), the lattice-diamond model presented an outstanding performance amongst the eight models. In addition, the lattice-diamond model, due to its architecture, only possesses convex surfaces, which may contribute to osteogenic differentiation enhancement of human MSCs [51].

It is worth noting that in this simulation study, we considered the cell culture medium as a Newtonian fluid, i.e. constant viscosity liquid, with no solid particles for simplification of the system of governing equations. Cell culture media involving serum may behave as a non-

Newtonian fluid and such shear rate dependent viscosity can cause changes in WSS distribution modality in the scaffolds [52]. It may be necessary to employ WSS quantification methods based on variable viscosity for studies involving non-Newtonian media.

5. Conclusion

We used CFD analysis to compare the permeability and the distribution statistics of fluid-induced WSS in high-porosity scaffolds, which are widely used in bone tissue engineering. Results of the study can be summarized as follows:

- The permeability of scaffolds is governed by their architecture and any changes in the size of channels (narrowing) reduce permeability. Therefore, scaffolds with a less variable pore size are more permeable.

- The ratio of the area with no obstacles to the total inlet area, A/A_0, plays a significant role in determining the permeability of the scaffolds in addition to $D/$d, which represents the ratio of the widest pore size to the narrowest.

- WSS and its distribution in the scaffold are influenced by the architecture of the scaffold.

- It is not possible to find a correlation between the architecture of the scaffolds and their WSS distribution statistics, which suggests that the design of scaffolds with the desired WSS distribution is not a straightforward task in tissue engineering.

- The results of this comparative study shed more light on the effective selection of architecture in the design of highly porous scaffolds.

References

1.   Chen, H.-C. and Y.-C. Hu, *Bioreactors for tissue engineering.* Biotechnology Letters, 2006. **28**(18): p. 1415-1423.

2.	Cheng, G., et al., *Promoting osteogenic differentiation in pre-osteoblasts and reducing tibial fracture healing time using functional nanofibers.* Nano Research, 2018. **11**(7): p. 3658-3677.

3.	Sierra-Sanchez, A., et al., *Epithelial In vitro Differentiation of Mesenchymal Stem Cells.* Current Stem Cell Research & Therapy, 2018. **13**(6): p. 409-422.

4.	Miyashita, S., et al., *Mechanical forces induce odontoblastic differentiation of mesenchymal stem cells on three-dimensional biomimetic scaffolds.* Journal of Tissue Engineering and Regenerative Medicine, 2017. **11**(2): p. 434-446.

5.	Yang, F., et al., *Combinatorial Extracellular Matrices for Human Embryonic Stem Cell Differentiation in 3D.* Biomacromolecules, 2010. **11**(8): p. 1909-1914.

6.	Prendergast, P.J., R. Huiskes, and K. Søballe, *Biophysical stimuli on cells during tissue differentiation at implant interfaces.* Journal of Biomechanics, 1997. **30**(6): p. 539-548.

7.	Maul, T.M., et al., *Mechanical stimuli differentially control stem cell behavior: morphology, proliferation, and differentiation.* Biomech Model Mechanobiol, 2011. **10**(6): p. 939-53.

8.	Govey, P.M., A.E. Loiselle, and H.J. Donahue, *Biophysical Regulation of Stem Cell Differentiation.* Current Osteoporosis Reports, 2013. **11**(2): p. 83-91.

9.	David, B., et al., *A Perfusion Bioreactor for Engineering Bone Constructs: An In Vitro and In Vivo Study.* Tissue Engineering Part C-Methods, 2011. **17**(5): p. 505-516.

10.	Toh, Y.-C. and J. Voldman, *Fluid shear stress primes mouse embryonic stem cells for differentiation in a self-renewing environment via heparan sulfate proteoglycans transduction.* The FASEB Journal, 2011. **25**(4): p. 1208-1217.

11. Ahsan, T. and R.M. Nerem, *Fluid Shear Stress Promotes an Endothelial-Like Phenotype During the Early Differentiation of Embryonic Stem Cells.* Tissue Eng Part A, 2010. **16**(11): p. 3547-53.

12. Sargent, C.Y., et al., *Hydrodynamic modulation of embryonic stem cell differentiation by rotary orbital suspension culture.* Biotechnology and Bioengineering, 2010. **105**(3): p. 611-626.

13. Adamo, L., et al., *Biomechanical forces promote embryonic haematopoiesis.* Nature, 2009. **459**(7250): p. 1131-5.

14. Delaine-Smith, R.M. and G.C. Reilly, *Mesenchymal stem cell responses to mechanical stimuli.* Muscles Ligaments Tendons J, 2012. **2**(3): p. 169-80.

15. Melchels, F.P.W., et al., *The influence of the scaffold design on the distribution of adhering cells after perfusion cell seeding.* Biomaterials, 2011. **32**(11): p. 2878-2884.

16. Li, Y., et al., *The effect of mechanical loads on the degradation of aliphatic biodegradable polyesters.* Regenerative Biomaterials, 2017. **4**(3): p. 179-190.

17. Katritsis, D., et al., *Wall Shear Stress: Theoretical Considerations and Methods of Measurement.* Progress in Cardiovascular Diseases, 2007. **49**(5): p. 307-329.

18. Amili, O., et al., *Evaluation of a film-based wall shear stress measurement technique in a turbulent channel flow.* Experimental Thermal and Fluid Science, 2016. **70**: p. 437-442.

19. Liu, X., Z. Li, and N. Gao, *An improved wall shear stress measurement technique using sandwiched hot-film sensors.* Theoretical and Applied Mechanics Letters, 2018. **8**(2): p. 137-141.

20. Ali, D. and S. Sen, *Permeability and fluid flow-induced wall shear stress of bone tissue scaffolds: Computational fluid dynamic analysis using Newtonian and non-*

Newtonian blood flow models. Computers in Biology and Medicine, 2018. **99**: p. 201-208.

21.   Ali, D. and S. Sen, *Finite element analysis of mechanical behavior, permeability and fluid induced wall shear stress of high porosity scaffolds with gyroid and lattice-based architectures.* Journal of the Mechanical Behavior of Biomedical Materials, 2017. **75**: p. 262-270.

22.   Ali, D. and S. Sen, *Finite element analysis of boron nitride nanotubes' shielding effect on the stress intensity factor of semielliptical surface crack in a wide range of matrixes using RVE model.* Composites Part B-Engineering, 2017. **110**: p. 351-360.

23.   Gómez, S., et al., *Design and properties of 3D scaffolds for bone tissue engineering.* Acta Biomaterialia, 2016. **42**: p. 341-350.

24.   Marin, A.C. and D. Lacroix, *The inter-sample structural variability of regular tissue-engineered scaffolds significantly affects the micromechanical local cell environment.* Interface Focus, 2015. **5**(2): p. 8.

25.   Thondapu, V., et al., *Endothelial shear stress 5 years after implantation of a coronary bioresorbable scaffold.* European Heart Journal, 2018. **39**(18): p. 1602-+.

26.   Truscello, S., et al., *Prediction of permeability of regular scaffolds for skeletal tissue engineering: A combined computational and experimental study.* Acta Biomaterialia, 2012. **8**(4): p. 1648-1658.

27.   Lesman, A., Y. Blinder, and S. Levenberg, *Modeling of Flow-Induced Shear Stress Applied on 3D Cellular Scaffolds: Implications for Vascular Tissue Engineering.* Biotechnology and Bioengineering, 2010. **105**(3): p. 645-654.

28.   Zhao, F.H., T.J. Vaughan, and L.M. McNamara, *Quantification of fluid shear stress in bone tissue engineering scaffolds with spherical and cubical pore architectures.* Biomechanics and Modeling in Mechanobiology, 2016. **15**(3): p. 561-577.

29.   Dias, M.R., et al., *Permeability analysis of scaffolds for bone tissue engineering.* Journal of Biomechanics, 2012. **45**(6): p. 938-944.

30.   Torres-Sanchez, C., J. McLaughlin, and A. Fotticchia, *Porosity and pore size effect on the properties of sintered Ti35Nb4Sn alloy scaffolds and their suitability for tissue engineering applications.* Journal of Alloys and Compounds, 2018. **731**: p. 189-199.

31.   Al-Ketan, O., R. Rowshan, and R.K. Abu Al-Rub, *Topology-mechanical property relationship of 3D printed strut, skeletal, and sheet based periodic metallic cellular materials.* Additive Manufacturing, 2018. **19**: p. 167-183.

32.   Rodríguez-Montaño, Ó.L., et al., *Comparison of the mechanobiological performance of bone tissue scaffolds based on different unit cell geometries.* Journal of the Mechanical Behavior of Biomedical Materials, 2018. **83**: p. 28-45.

33.   Egan, P.F., et al., *Computationally designed lattices with tuned properties for tissue engineering using 3D printing.* Plos One, 2017. **12**(8).

34.   Sercombe, T.B., et al., *Failure modes in high strength and stiffness to weight scaffolds produced by Selective Laser Melting.* Materials & Design, 2015. **67**: p. 501-508.

35.   Van Bael, S., et al., *The effect of pore geometry on the in vitro biological behavior of human periosteum-derived cells seeded on selective laser-melted Ti6Al4V bone scaffolds.* Acta Biomaterialia, 2012. **8**(7): p. 2824-2834.

36.   Rittman, M., et al., *Direct visualisation of lipid bilayer cubic phases using Atomic Force Microscopy.* Soft Matter, 2010. **6**(17): p. 4058-4061.

37.   Blanquer, S.B.G., et al., *Surface curvature in triply-periodic minimal surface architectures as a distinct design parameter in preparing advanced tissue engineering scaffolds.* Biofabrication, 2017. **9**(2).

38.   Lee, H.G. and J. Kim, *Regularized Dirac delta functions for phase field models.* International Journal for Numerical Methods in Engineering, 2012. **91**(3): p. 269-288.

39. Yoo, D.-J., *Computer-aided porous scaffold design for tissue engineering using triply periodic minimal surfaces.* International Journal of Precision Engineering and Manufacturing, 2011. **12**(1): p. 61-71.

40. Vossenberg, P., et al., *Darcian permeability constant as indicator for shear stresses in regular scaffold systems for tissue engineering.* Biomechanics and Modeling in Mechanobiology, 2009. **8**(6): p. 499.

41. Xue, X., et al., *Analysis of fluid separation in microfluidic T-channels.* Applied Mathematical Modelling, 2012. **36**(2): p. 743-755.

42. Egger, D., et al., *Development and Characterization of a Parallelizable Perfusion Bioreactor for 3D Cell Culture.* Bioengineering, 2017. **4**(2): p. 51.

43. Gooch, J.W., *Hagen-Poiseuille Equation*, in *Encyclopedic Dictionary of Polymers*, J.W. Gooch, Editor. 2011, Springer New York: New York, NY. p. 355-355.

44. Sinha, R., et al., *Endothelial cell alignment as a result of anisotropic strain and flow induced shear stress combinations.* Scientific Reports, 2016. **6**.

45. Voronov, R., et al., *Computational modeling of flow-induced shear stresses within 3D salt-leached porous scaffolds imaged via micro-CT.* Journal of Biomechanics, 2010. **43**(7): p. 1279-1286.

46. Li, D.Q., et al., *Effects of Flow Shear Stress and Mass Transport on the Construction of a Large-Scale Tissue-Engineered Bone in a Perfusion Bioreactor.* Tissue Engineering Part A, 2009. **15**(10): p. 2773-2783.

47. Olivares, A.L., et al., *Finite element study of scaffold architecture design and culture conditions for tissue engineering.* Biomaterials, 2009. **30**(30): p. 6142-6149.

48. Zhao, F., T.J. Vaughan, and L.M. McNamara, *Multiscale fluid-structure interaction modelling to determine the mechanical stimulation of bone cells in a tissue engineered scaffold.* Biomech Model Mechanobiol, 2015. **14**(2): p. 231-43.

49. Ochoa, I., et al., *Permeability evaluation of 45S5 Bioglass®-based scaffolds for bone tissue engineering.* Journal of Biomechanics, 2009. **42**(3): p. 257-260.

50. Rahbari, A., et al., *Predicting permeability of regular tissue engineering scaffolds: scaling analysis of pore architecture, scaffold length, and fluid flow rate effects.* Computer Methods in Biomechanics and Biomedical Engineering, 2017. **20**(3): p. 231-241.

51. Werner, M., et al., *Surface Curvature Differentially Regulates Stem Cell Migration and Differentiation via Altered Attachment Morphology and Nuclear Deformation.* Advanced Science, 2017. **4**(2).

52. Wyma, A., et al., *Non-Newtonian rheology in suspension cell cultures significantly impacts bioreactor shear stress quantification.* Biotechnology and Bioengineering, 2018. **115**(8): p. 2101-2113.

Highlights:

- Minimal surface and lattice-based architectures exhibit different flow behavior
- Scaffold permeability can vary up to three times depending on the architecture
- Scaffolds with minimal variation in channel size exhibit the highest permeability
- Wall shear stress distribution does not correlate with scaffold architecture
- Scaffold design with desired wall shear stress distribution is problematical
- Architecture selection in designing highly porous scaffolds will affect bioactivity